# Multifunctionality of Layered Materials

Septiany, Liany

*DOI:*
10.33612/diss.182500502

# Chapter 3

## Thermoelectric Properties and Phase Evolution of $(GeSe)_{1-x}(AgBiTe_2)_x$

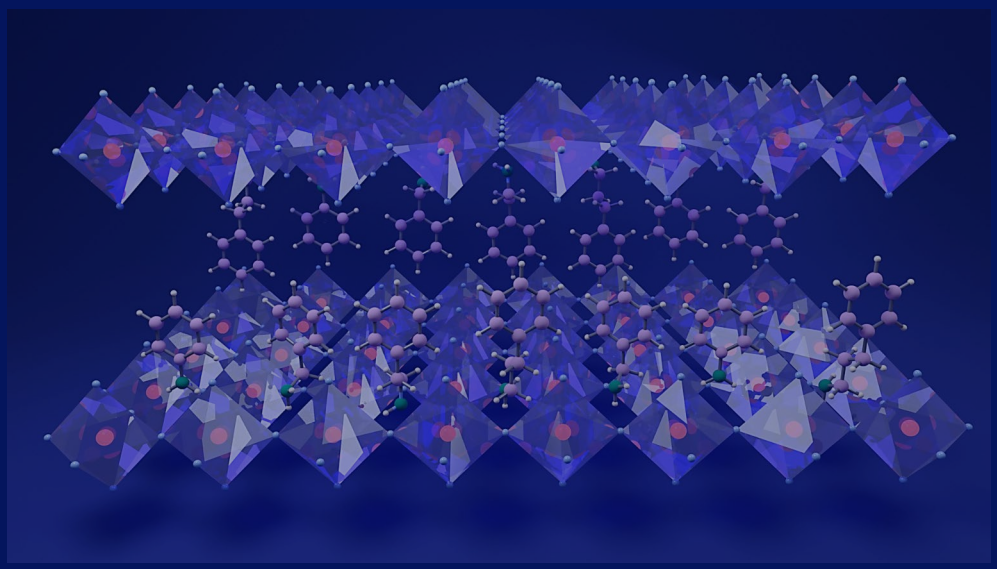

L. Septiany, J. Baas, G.R. Blake

*Thermoelectric Properties and Phase Evolution of $(GeSe)_{1-x}(AgBiTe_2)_x$*

*In Preparation*

## Abstract

Orthorhombic GeSe is known for its predicted ultra-low thermal conductivity (~0.34 W/mK), but the carrier concentration remains low ($<10^{18}$ $cm^{-3}$) even after the introduction of dopants, resulting in poor thermoelectric performance. When GeSe is alloyed with $AgBX_2$ (B = Sb, Bi; X = Se, Te), the entropy of the system is enhanced, leading to a higher symmetry rhombohedral (distorted rocksalt) phase. This phase exhibits much better thermoelectric performance due to a change in band structure which leads to a significant increase in electrical conductivity. Here we report on a new series of $(GeSe)_{1-x}(AgBiTe_2)_x$ alloys ($0 \le x \le 0.3$) which exhibit ZT values of up to 0.93 at 680 K for x = 0.15, with an average ZT of ~0.66 over the temperature range 300-680 K. The high ZT is achieved due to lower thermal conductivity caused by atomic mass disorder introduced by the heavy element Bi, while the electrical conductivity and Seebeck coefficient remain comparable to other GeSe-$AgBX_2$ materials. We also study the evolution of microstructure and phase distribution in the samples after thermal treatment.


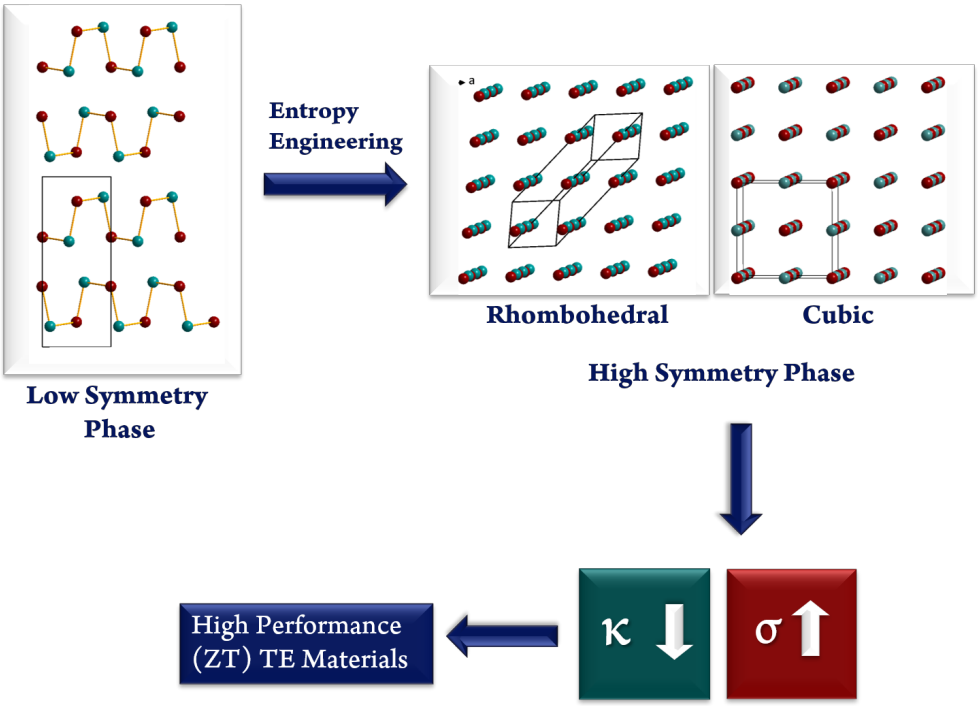

## 3.1 Introduction

The depletion of our planet's fossil fuels and the ongoing climate crisis has become increasingly alarming, forcing us to use energy in a more sustainable manner. In this respect, the recovery of waste heat that can be converted to electricity using thermoelectric materials has gained much attention in recent years.[1–4] Industrial processes, vehicle exhaust systems and home heating are just a few examples of many sources that produce waste heat. The energy conversion efficiency of thermoelectric materials is directly related to the figure of merit (ZT) which depends on several conflicting properties: Seebeck coefficient $S$, electrical conductivity $\sigma$, and thermal conductivity $\kappa$, which is the sum of electronic ($\kappa_e$) and lattice ($\kappa_l$) contributions.[5,6] Enhancement of ZT can be achieved by either maximizing the power factor $S^2\sigma$ or minimizing $\kappa$. An increased power factor can be realized by carrier concentration optimization[7], band engineering[8–10] and introducing resonant levels by chemical doping[11–13]. Reduced thermal conductivity, in particular the $\kappa_l$ component, can be achieved by solid-solution alloying,[14] especially using elements with large atomic mass contrast, utilizing materials with intrinsically low thermal conductivity, and designing all-scale hierarchical architectures[15–17]. In general, the nanostructuring of materials with high power factors leads to a high density of interfaces that scatter heat-carrying phonons, reducing $\kappa_l$ while maintaining good electronic properties and thus enhancing ZT.[14,18]

The family of IV-VI semiconductor materials is widely known for their excellent thermoelectric properties;[19,20] for example, previous studies have reported high ZT values for PbTe, SnSe, GeTe, and IV-VI-based alloys such as TAGS and LAST.[21–27] Single crystals of SnSe demonstrated a record high ZT of ~2.6 at 973 K along the *b*-axis, mainly due to an ultra-low thermal conductivity of ~0.35 $Wm^{-1}K^{-1}$ along this axis above 600 K.[28] As an analogous compound with a similar orthorhombic structure, GeSe has also begun to attract attention,[29] although studies on this material are still rather scarce. At an optimum carrier concentration of ~$5\times10^{19}$ $cm^{-3}$, ZT values of higher than 2.0 above 600 K have been theoretically predicted for p-doped materials.[29] Based on the predicted power factor, n-doped GeSe with a carrier concentration in the ~$10^{20}$ $cm^{-3}$ range might exhibit even better performance.[31] A thermal conductivity of ~0.40 $Wm^{-1}K^{-1}$ at 700 K was measured for polycrystalline samples of GeSe doped with Ag,[32] in good agreement with values predicted for

the pristine, single crystalline material.[29] However, the highest carrier concentration that has been experimentally reported is ~$10^{18}$ $cm^{-3}$ for Ag-doping, and the doping limit in this structure type appears to be too low to reach the optimal carrier concentration necessary for good thermoelectric performance.[29,30]

Recent work has reported that the orthorhombic phase is transformed to a rhombohedral structure when GeSe is alloyed with $AgBX_2$ (B= Sb, Bi; X=Se, Te),[31–33] resulting in a p-type thermoelectric material that shows a significant improvement in performance. The higher symmetry rhombohedral structure possesses a modified band structure with a multi-valley Fermi surface. Thus, the phase transformation leads to a significant increase in carrier concentration that cannot be achieved by single element doping[31,32]. Furthermore, a large proportion of atomic substitutions on equivalent lattice sites leads to increased configurational entropy and an enhanced potential for higher crystal symmetry to be stabilized.[34,35] For example, high symmetry *bcc* or *fcc* phases are stabilized in alloys and oxides when at least five substituted components with large differences in atomic size and electronegativity are present.[35,36] Entropy engineering may lead to the enhancement of ZT in two possible ways. Multicomponent systems with high entropy exhibit atomic mass disorder and point defects, increasing the degree of phonon scattering and significantly reducing the lattice thermal conductivity. Furthermore, alloying can tune the crystal field and promote convergence between the lower light and higher heavy valence bands. The raising of the light valence band maximum increases both the density of states effective mass and carrier mobility, leading to a significantly improved power factor.[35] Both of these considerations are expected to enhance the ZT value.

Such an entropy engineering strategy has previously been utilized to obtain a ZT of 0.96 at ~700 K in $(GeSe)_{0.8}(AgSbTe_2)_{0.2}$ due to both a higher carrier concentration ($8.9 \times 10^{19}$ $cm^{-3}$) than can be obtained by single-component doping of GeSe, and to a low thermal conductivity of ~0.7 W/mK.[32] In this report, we present a new series of alloys $(GeSe)_{1-x}(AgBiTe_2)_x$ which show low thermal conductivities of between 0.4 and 0.8 W/mK above 600 K. We demonstrate that a maximum ZT of 0.93 is achieved at 680 K for the $x = 0.15$ composition.

## 3.2 Experimental Details

### 3.2.1 Synthesis

A series of $(GeSe)_{1-x}(AgBiTe_2)_x$ samples was synthesized with $x$ = 0, 0.05, 0.1, 0.15, 0.2, and 0.3. High purity powders of Ge, Se, Ag, Bi, and Te (99.999%) were weighed in a nitrogen atmosphere glove-box in stoichiometric proportions for a total mass of 10 g. The mixed powder was then ball-milled for 12 h at 250 rpm and loaded into a carbon-coated quartz tube. Subsequently, the tube was flame-sealed under vacuum, slowly heated to 1223 K and held for 6 h. Finally, the tube was quenched to room temperature before annealing at 1023 K for another 6h.

### 3.2.2 Powder X-Ray Diffraction

The ingots were hand-ground into a fine powder using an agate mortar and pestle for X-ray diffraction (XRD) measurements, which were carried out using a Bruker D8 Advance diffractometer equipped with a Cu-Kα (λ= 1.5406 Å) source. The structural parameters were determined by Rietveld refinement using the GSAS software.[37]

### 3.2.3 Thermoelectric Properties Measurements

For thermal diffusivity, Seebeck coefficient, and electrical conductivity measurements, the obtained ingots were cut to a rectangular shape and polished. Thermal diffusivity (D) was measured using the laser flash method in a Linseis LFA 500; the heat capacity was calculated using the equation $C_p$ (GeSe, (298.15-940) K) = $((46.777 + 15.099) \times 10^{-3}T - 0.0316 \times 10^{-6} T^2 - 1.231 \times 10^5 T^{-2})$ J $K^{-1}$ $mol^{-1}$.[38] The thermal conductivity was then calculated using $\kappa = \rho D C_p$, where the density ρ was estimated by measuring the mass and dimensions of the sample. The densities of all samples are ≥ 94% of the theoretical density.

The electrical resistivity and Seebeck coefficient were measured simultaneously using Linseis LSR-3 equipment, which utilizes a dc four-probe method. The carrier concentration was determined by Hall measurement using the 4-probe van der Pauw method. Contacts were made to rectangular shaped samples using silver-paste and gold wires. The measurement employed a

Keithley 237 current source and an Agilent 3458A multimeter in a Quantum Design Physical Properties Measurement System (PPMS).

### 3.2.4 Scanning Electron Microscope (SEM) Measurements

The microstructure was studied by high-resolution scanning electron microscopy (SEM) in a FEI Nova NanoSEM, equipped with an energy-dispersive X-Ray spectrometer (EDS). The SEM sample was prepared from the ingot by encapsulation in a bakelite mold, which was then polished until the microstructure could be observed under an optical microscope.



## 3.3 Results and Discussion

### 3.3.1 Structural Analysis

Fig. 3.1b shows room temperature powder XRD patterns of the $(GeSe)_{1-x}(AgBiTe_2)_x$ alloys synthesized in this report. Pristine GeSe has an orthorhombic layered structure (space group *Pnma*) under ambient conditions and is known to undergo a phase transition to a cubic rocksalt structure (space group $Fm\bar{3}m$) at 920-930K.[39,40] Our XRD patterns show that structural changes also occur with increasing $AgBiTe_2$ concentration, first from orthorhombic (*Pnma*) to rhombohedral (*R3m*) and then to cubic symmetry ($Fm\bar{3}m$). The rhombohedral structure is closely related to the cubic rocksalt structure by opposite shifts of adjacent (111) cation/anion layers such that the cubic unit cell is elongated along one of the four [111] body diagonals. This rhombohedral structure can also be represented in a hexagonal setting (shown in Fig. 3.1a) where alternating cation and anion layers are stacked along the hexagonal *c*-axis. The rhombohedral structure emerges at $x = 0.05$ and coexists with the orthorhombic phase, whereas at $x = 0.1$ a single rhombohedral phase is observed. With increasing $x$ the rhombohedral distortion gradually decreases, as evidenced by the doublet of 211 and 101,¯ peaks at ~44° which gradually move closer together. The doublet has merged to a single peak for $x = 0.3$, indicating a pure cubic phase. Increasing the concentration of a second component in a matrix system, in this case $AgBiTe_2$ in a GeSe matrix, tends to stabilize a higher symmetry structure, as often observed in high entropy alloy systems.[37]

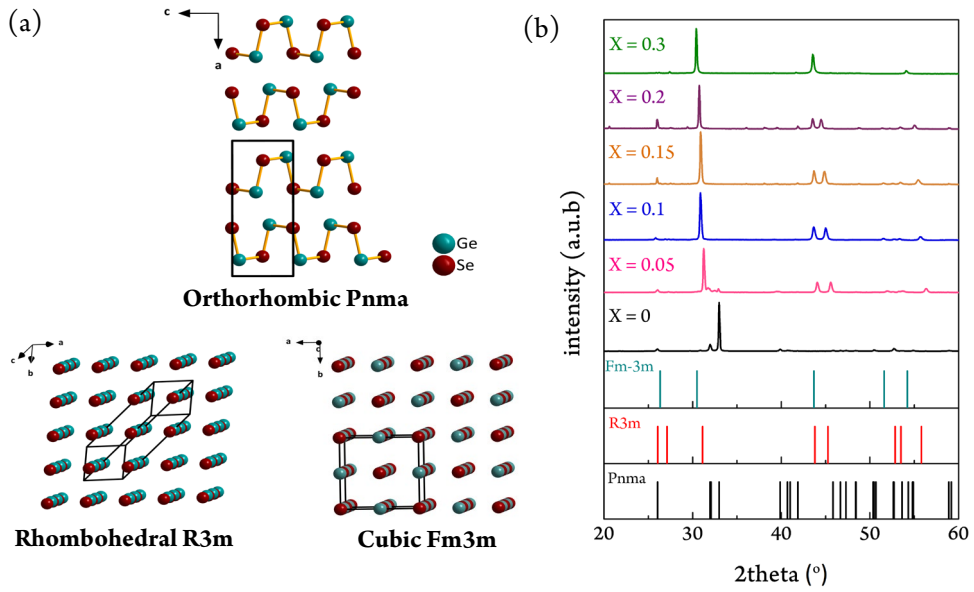


***Figure 3.1*** *(a) Schematic of orthorhombic (space group Pnma), rhombohedral (R3m) and cubic ($Fm\bar{3}m$) crystal structures of GeSe. Unit cells are outlined, in the hexagonal setting in the case of the rhombohedral structure. (b) Room temperature powder XRD patterns of $(GeSe)_{1-x}(AgBiTe_2)_x$ ($x$ = 0, 0.05, 0.1, 0.15, 0.2 and 0.3).*

With increasing $AgBiTe_2$ concentration, the XRD peaks are shifted to lower angle as the lattice expands (Table 3.1). The lattice parameters increase smoothly with $AgBiTe_2$ concentration when $x \geq 0.05$, implying that the larger $Ag^+$ and $Bi^{3+}$ cations are substituted on the $Ge^{2+}$ position in the crystal structure (note that these oxidation states are nominal – the bonding in these materials is not fully ionic). Fits to the XRD patterns of all the samples are shown in Fig. 3.2.

Weak peaks corresponding to a minor impurity phase are observed in the XRD patterns of all the alloyed samples, and could not be indexed according to any known phase. These peaks become more pronounced for higher alloy concentrations ($x$ > 10%). The impurity is obvious in back-scattered electron SEM images of all the samples as precipitates of light contrast and sizes sometimes larger than 10 μm (Fig 3.2, Appendix, Fig. 3.10), situated in particular at grain boundaries. EDS measurements show that the precipitates are silver-rich with approximate composition $Ge_{0.5}Se\text{-}AgTe_{0.6}$.

**Table 3.1** Lattice parameters of as prepared $(GeSe)_{1-x}(AgBiTe_2)_x$ samples.

| Sample | Space Group | Lattice Parameters | | | |
|---|---|---|---|---|---|
| | | a (Å) | b (Å) | c (Å) | V (Å$^3$) |
| x = 0 | Orthorhombic *Pnma* | 10.8304(4) | 3.8363(2) | 4.3922(3) | 182.49(2) |
| x = 5% | Orthorhombic *Pnma* | 10.9115(6) | 3.9517(3) | 4.3389(4) | 187.09(2) |
| | Rhombohedral *R3m* | 3.9745(3) | 3.9745(3) | 10.2239(9) | 139.79(2) |
| x = 10% | Rhombohedral *R3m* | 4.0127(2) | 4.0127(2) | 10.2682(5) | 143.19(1) |
| x = 15% | Rhombohedral *R3m* | 4.0437(2) | 4.0437(2) | 10.2683(5) | 145.68(2) |
| x = 20% | Rhombohedral *R3m* | 4.0761(2) | 4.0761(2) | 10.2970(8) | 148.16(2) |
| x = 30% | Cubic $Fm\bar{3}m$ | 5.8675(2) | 5.8675(2) | 5.8675(2) | 202.01(2) |

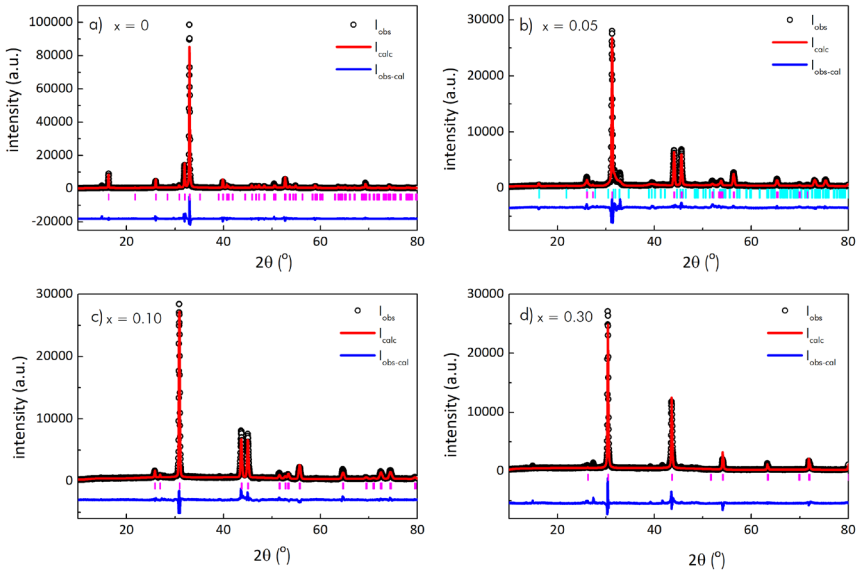


***Figure 3.2*** *Observed (black circles), fitted (red line) and difference (blue line) room temperature PXRD patterns of $(GeSe)_{1-x}(AgBiTe_2)_x$. Markers under the profiles show the allowed reflection positions. a) x = 0, orthorhombic Pnma; b) x = 0.05, coexisting orthorhombic Pnma and rhombohedral R3m phases; c) x = 0.10, rhombohedral R3m; d) x = 0.30, cubic $Fm\bar{3}m$.*

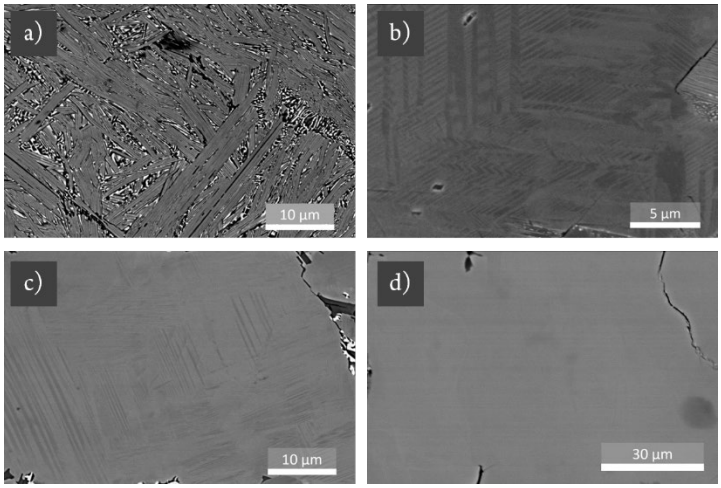


***Figure 3.3*** *SEM images of (a) x = 0.05, (b) x = 0.10, (c) x = 0.15, and (d) x = 0.20 samples.*

We analyzed the microstructures of the samples using SEM. Fig. 3.3 shows the microstructure of the as-prepared $x$ = 0.05, 0.10, 0.15, and 0.20 samples. The $x$ = 0.10 and 0.15 samples exhibit the typical "herringbone" sub-micron domain structure of rhombohedral IV-VI semiconductors (Fig. 3.3b), previously observed for example in GeTe.[41] Further SEM images of all the sample are shown in the Appendix, Fig. 3.10. However, this domain structure is absent for the x = 0.05 sample in which the orthorhombic phase is formed alongside the rhombohedral phase, giving a chemically phase-separated lamellar microstructure as depicted in Fig. 3.3a. The strong contrast between dark and light lamellae suggests that chemical phase separation into orthorhombic GeSe-rich and rhombohedral/trigonal $AgBiTe_2$-rich phases occurs, the latter having a much larger average atomic mass than the former. This observation is consistent with the phase segregation apparent in the XRD patterns (Fig. 3.2b). The widths of the lamellae are smaller than the resolution of the EDS probe, thus we were unable to determine the compositions of the dark and light areas. This type of microstructure has not previously been reported for GeSe-based materials. However, Ikeda et al. found similar self-assembled lamellae in the PbTe-$Sb_2Te_3$ system and demonstrated that these features lower the thermal conductivity due to the interface effect between the two phases which increases the phonon scattering.[42]

### 3.3.2 Thermoelectric Properties

Pristine GeSe has a high Seebeck coefficient of 597 μV/K at room temperature (Fig. 3.4a), which is typical for a p-type semiconductor with low carrier concentration. The Seebeck coefficient drops significantly after the introduction of 5% $AgBiTe_2$ in the alloyed samples but then increases with $AgBiTe_2$ content up to 30%, a trend that does not simply follow that of the carrier concentration (Table 3.2), suggesting a higher electronic density of states and effective mass on alloying (at least up to 15%) as expected for a high-entropy system.[34] A broad maximum in the *S* versus *T* plot is observed for all compositions except $x = 0.3$, which might be due to a temperature-induced structural phase transition to the cubic rocksalt phase as reported for the analogous system GeSe-$AgSbTe_2$.[32] The position of this maximum shifts to lower temperature with increasing *x*, probably due to the decreasing degree of rhombohedral distortion.

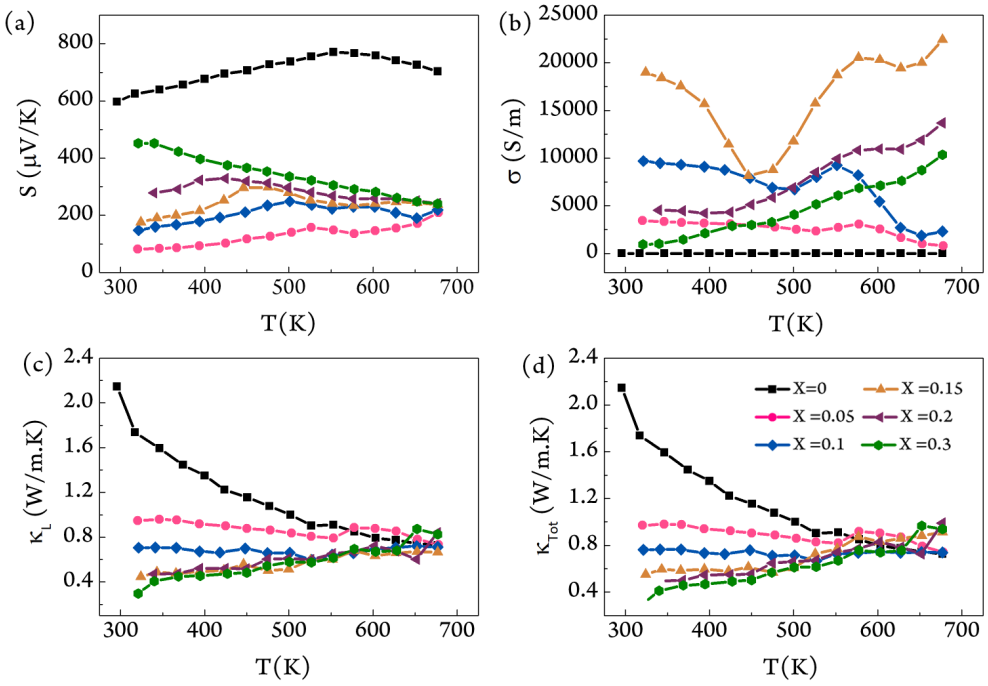


***Figure 3.4*** *a) Seebeck coefficient, b) electrical conductivity, c) lattice contribution to thermal conductivity and d) total thermal conductivity as a function of temperature for* $(GeSe)_{1-x}(AgBiTe_2)_x$ *samples.*

As observed for other GeSe-$AgBX_2$ alloys[31–33], the electrical conductivity of rhombohedral GeSe is superior to that of the orthorhombic phase (Fig. 3.4b). Band structure studies have shown that rhombohedral GeSe has both a higher carrier effective mass and a Fermi surface with more conducting pockets, thus is expected to show both improved electrical conductivity and a higher Seebeck coefficient.[32] It has also been argued that similar to rhombohedral GeTe, the rhombohedral phase of GeSe has a high concentration of Ge vacancies, creating more holes and resulting in an increased carrier concentration.[36] The electrical conductivity of $(GeSe)_{1-x}(AgBiTe_2)_x$ increases with x until a maximum is reached at $x = 0.15$ and then decreases for larger $x$. This is consistent with the trend in carrier concentration (Table 3.2), which increases with $x$ until it reaches a maximum of $3.13 \times 10^{19}$ $cm^{-3}$ at $x = 0.15$. Since $Bi^{3+}$ is an electron donor,[36] it will compensate some of the Ge vacancies created in the rhombohedral phase, leading to a lower carrier concentration as $x$ is increased further. For $x = 0.05$, the carrier concentration is significantly lower than reported for other GeSe-$AgBX_2$ alloys[31–33], probably due to the mixed orthorhombic and rhombohedral phases that coexist at this alloying concentration.

$(GeSe)_{1-x}(AgBiTe_2)_x$ with $x = 0.05$ and 0.1 both show a decrease in electrical conductivity with increasing temperature up to ~500K, indicating highly-degenerate semiconducting behavior; the sharp increase between 500 and 600 K might be due to the expected structural phase transition between the rhombohedral and high temperature cubic phases [32]. In contrast, for the alloys with x = 0.15, 0.2 and 0.3, the electrical conductivity increases with temperature suggesting a non-degenerate semiconducting nature. The electrical conductivity of pristine GeSe reaches a maximum of 0.69 S/m at 680 K, while $(GeSe)_{1-x}(AgBiTe_2)_x$ exhibits a maximum value of 22400 S/m at 677 K for x = 0.15.

**Table 3.2**. Hall carrier concentration of $(GeSe)_{1-x}(AgBiTe_2)_x$ (x = 0.05, 0.1, 0.15, 0.2 and 0.3) measured at 300 K

| Sample | Carrier concentration ($cm^{-3}$) |
|---|---|
| **x = 0[32]** | $4.29 \times 10^{14}$ |
| **x = 5%** | $5.06 \times 10^{16}$ |
| **x = 10%** | $2.25 \times 10^{18}$ |
| **x = 15%** | $3.13 \times 10^{19}$ |
| **x = 20%** | $8.31 \times 10^{18}$ |
| **x = 30%** | $4.08 \times 10^{18}$ |

The total thermal conductivity of all our samples is dominated by the lattice contribution as seen in Fig. 3.4c and d. The lattice contribution is obtained by the subtraction of $\kappa_e$ (the electronic contribution) from $\kappa_{tot}$, such that $\kappa_{tot} = \kappa_e + \kappa_l$. The value of $\kappa_e$ is calculated from *Weidemann-Franz* law $\kappa_e = L\sigma T$, where L is the Lorentz number, $\sigma$ is the electrical conductivity and T is the temperature. The Lorentz number is calculated from the equation

$$L = 1.5 + \exp[-\frac{|S|}{116}] \quad (1)$$

which is valid for non-degenerate semiconductors and is often used for chalcogenide compounds.[43] The expression estimates L in units of $10^{-8}$ W.ohm/K when the Seebeck coefficient S is given in units of μV/K. $\kappa_e$ is plotted versus T in Fig. 3.5 The measured $\kappa_{tot}$ of pristine GeSe (Fig. 3.4d) is 2.14 W/mK at 300 K and decreases to 0.78 W/mK at 680 K, which agrees with previous reports.[33,44] Below ~600 K, $\kappa_{tot}$ for all the $(GeSe)_{1-x}(AgBiTe_2)_x$ alloys is significantly lower than the pristine sample. In contrast to the pristine sample, which exhibits a strong temperature dependence of $\kappa_L$ as often observed for crystalline materials, the trend in the alloys is much flatter which suggests phonon glass-like behavior. The $\kappa_{tot}$ for the alloys is in the range 0.4 – 1.0 W/mK at 680 K.

The suppressed lattice thermal conductivity of the alloyed samples can be attributed to impurity / point defect scattering or atomic mass disorder[34] associated with both the cation and anion sites. The presence of Ag-rich precipitates does not appear to play a significant role in phonon scattering, probably because they are generally larger than the phonon mean free path. In addition, the lamellae observed in the microstructure of the orthorhombic phase do not appear to lower the thermal conductivity further.

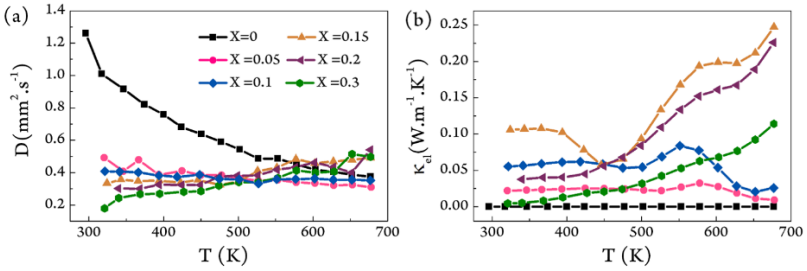


***Figure 3.5*** *Temperature dependent (a) thermal diffusivity and (b) electronic contribution to thermal conductivity of* $(GeSe)_{1-x}(AgBiTe_2)_x$ *(x = 0, 0.05, 0.1, 0.15, 0.2 and 0.3).*

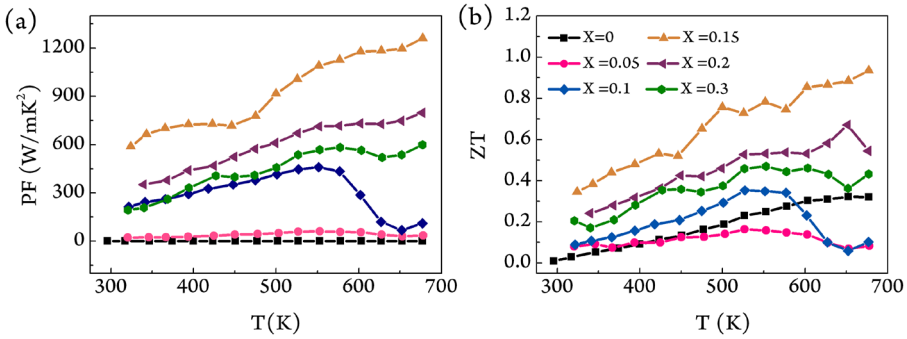


***Figure 3.6*** *Temperature dependence of (a) power factor and (b) ZT for* $(GeSe)_{1-x}(AgBiTe_2)_x$.

The power factors (PF) of all the $(GeSe)_{1-x}(AgBiTe_2)_x$ samples are significantly higher than that of the pristine sample throughout the temperature range measured (Fig. 3.6a) and for x = 0.15 the PF is comparable to the best performing GeSe alloy in previous reports, GeSe-$AgSbTe_2$[32]. The maximum PF of $(GeSe)_{0.85}(AgBiTe_2)_{0.15}$ is 1260 $W/mK^2$ at 680 K. The increase in PF and the suppression of $\kappa_{tot}$ over most of the temperature range results in significantly higher ZT values for the alloyed samples (Fig. 3.6b), the maximum ZT being 0.93 at 680 K, with $ZT_{ave}$ of 0.66, for $(GeSe)_{0.85}(AgBiTe_2)_{0.15}$. The thermoelectric properties presented in Fig 3.5 and 3.6 were measured after three heating and cooling cycles, after which the phase composition has stabilized (see discussion below).

### 3.3.3 Phase Evolution and Thermoelectric Properties after Thermal Treatment

We observed a significant degradation in the thermoelectric properties of $(GeSe)_{1-x}(AgBiTe_2)_x$ samples with x = 0.05 and 0.10 after thermal cycling. As depicted in Fig. 3.7a, for x = 0.10 the electrical conductivity greatly decreases from 32000 S/m to 3500 S/m at 300 K, suggesting that a significant change in the sample takes place. To probe the reasons for these changes in thermoelectric performance, especially in electrical conductivity, we further analyzed the powder XRD patterns and microstructure of as-prepared and thermally cycled samples.

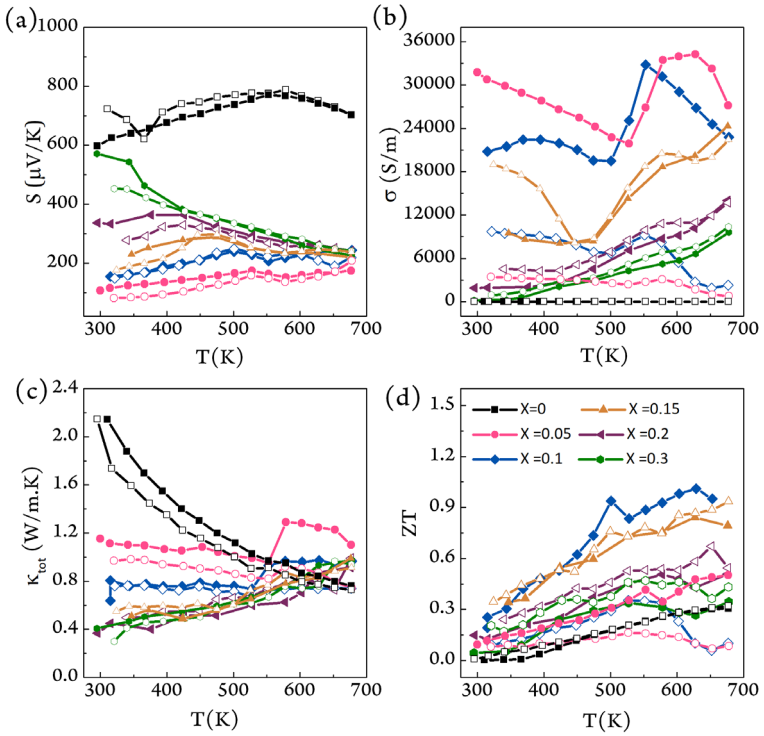


***Figure 3.7*** *(a) Seebeck coefficient, (b electrical conductivity, (c) total thermal conductivity, and (d) ZT values of* $(GeSe)_{1-x}(AgBiTe_2)_x$ *in first(solid symbols) and third (open symbols) heating cycles.*

Fig 3.8a and b show the evolution of the powder XRD patterns of $(GeSe)_{1-x}(AgBiTe_2)_x$ (x = 0.10 and x = 0.15) after two and three thermal cycles. Here thermal cycling was perfomed to mimic the heating and cooling processes during the measurement of thermoelectric properties. In each cycle the temperature was increased to 400˚C over 2h, held for 2h and then cooled down to room temperature. After two thermal cycles, peaks corresponding to the orthorhombic phase emerge alongside those of the initial rhombohedral phase for the x = 0.1 sample. The signature double-peak of the rhombohedral phase at ~44° is also suppressed. For x = 0.05, the fraction of orthorhombic phase that was already present becomes larger. It appears that annealing promotes phase segregation between GeSe and $AgBiTe_2$. However, these changes in phase distribution after thermal treatment are only observed for the x = 0.05 and 0.1 compositions; for the other alloying concentrations no major changes are observed, and all thermoelectric and structural properties remain essentially the same within experimental uncertainty, as presented in Fig.3.7.

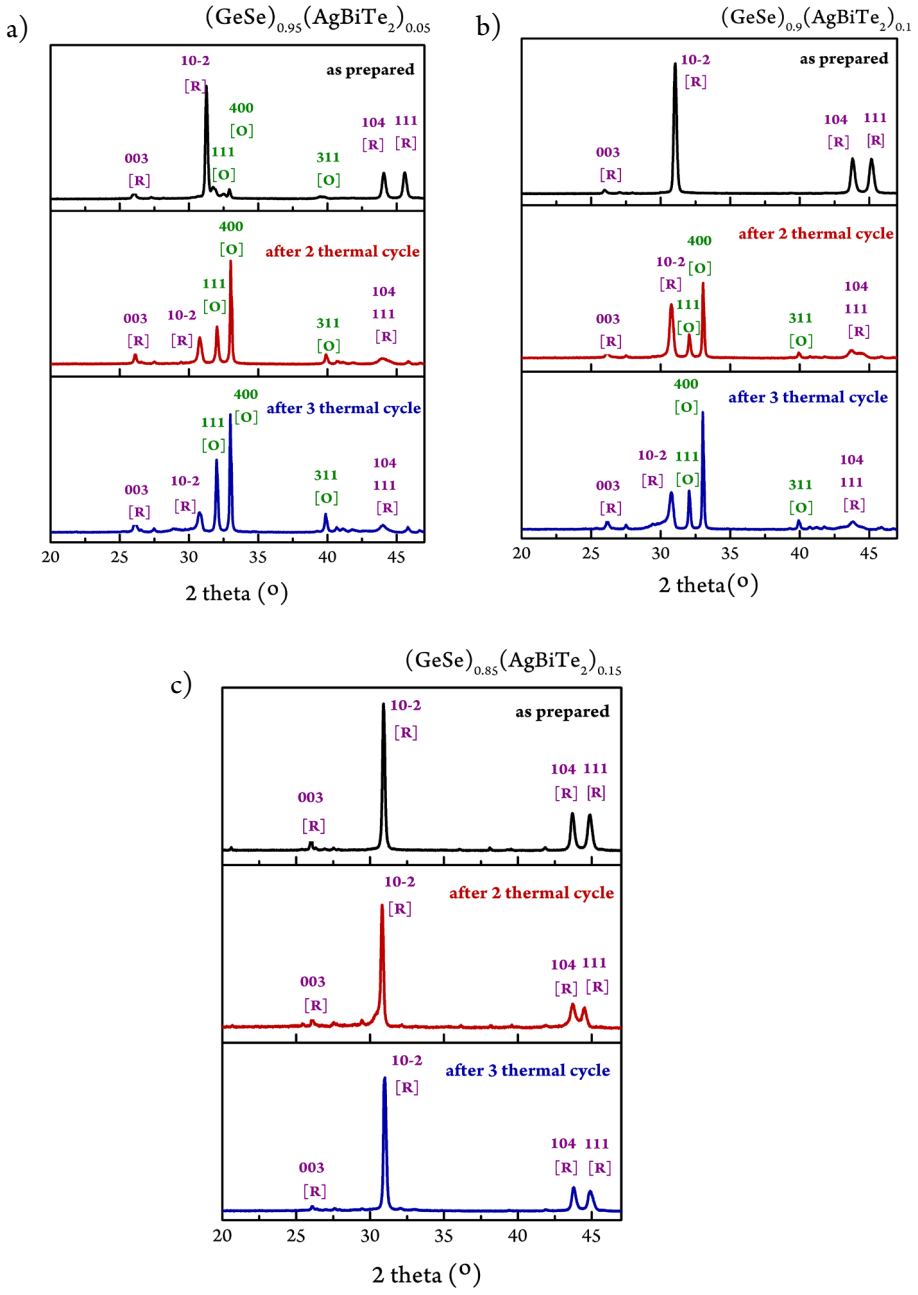


***Figure 3.8*** *Room temperature P-XRD patterns of $(GeSe)_{1-x}(AgBiTe_2)_x$, for (a) x =0.05, (b) x = 0.1 and (c) x = 0.15, in the as-prepared state and measured after 2 and 3 thermal cycles. The x = 0.1 sample shows new peaks after thermal cycling due to phase separation between orthorhombic GeSe-rich and rhombohedral $AgBiTe_2$-rich phases.*

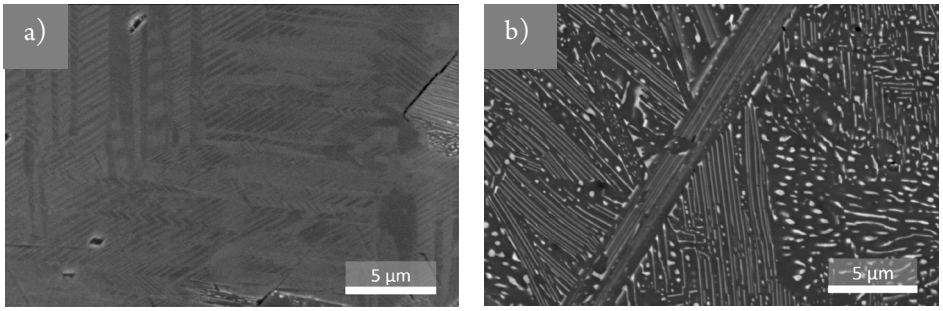


***Figure 3.9*** *SEM images of a) as-prepared $(GeSe)_{0.9}(AgBiTe2)_{0.1}$ and b) the same sample after thermal cycling. The lighter contrast indicates a $AgBiTe_2$ rich phase, while the darker contrast corresponds to a GeSe-rich phase.*

We also analyzed the microstructure of $(GeSe)_{0.9}(AgBiTe_2)_{0.1}$ after two thermal cycles as presented in Fig. 3.9. We observed further phase separation for the samples with x = 0.05 and 0.1. We found that for sample with x = 0.05 and 0.10. As suggested by the XRD data, we find the sample with x = 0.05 and 0.10 are metastable and undergo chemical phase separation to form a lamellar microstructure after heat treatment. The obvious contrast in the SEM image indicates that GeSe-rich and $AgBiTe_2$-rich lamellae are formed.

The phase separation observed is also consistent with the decrease in electrical conductivity for the x = 0.05 and 0.1 samples after thermal cycling. As discussed in the Introduction, the orthorhombic GeSe phase has poorer electrical transport properties than the rhombohedral and cubic structures. This is due to a combination of the lower concentration that can be stabilised in the orthorhombic structures and also the substantial differences in the electronic structure that lead to much better electrical conductivity in the rhombohedral phase [45]. The separation into orthorhombic and rhombohedral phases on the sub-micron scale will thus hinder electrical transport in the sample as a whole.

## 3.4 Conclusions

$(GeSe)_{1-x}(AgBiTe_2)_x$ alloys with $x$ = 0, 0.05, 0.1, 0.15, 0.2, and 0.3 were prepared from the melt. The pristine GeSe sample adopts a layered orthorhombic structure, while the introduction of 5% $AgBiTe_2$ induces the emergence of a rhombohedral (distorted rocksalt) structure alongside the orthorhombic phase; the former becomes dominant with further increasing $AgBiTe_2$ concentration. At a 30% fraction of $AgBiTe_2$, a cubic rocksalt phase is formed. The thermoelectric properties of $(GeSe)_{0.85}(AgBiTe_2)_{0.15}$ show a maximum ZT of 0.93 at 680 K and $ZT_{ave}$ of 0.66. The electrical conductivity is comparable to that of similar GeSe-based alloys, but the thermal conductivity of $(GeSe)_{1-x}(AgBiTe_2)_x$ is further suppressed due to more pronounced point defect and atomic mass disorder effects. In addition, $(GeSe)_{1-x}(AgBiTe_2)_x$ alloys with x= 0.05 and 0.1 undergo phase separation on the sub-micron scale to orthorhombic GeSe-rich and rhombohedral $AgBiTe_2$-rich phases after thermal treatment, leading to a significant decrease in the electrical conductivity and hence ZT.

Note: After this chapter was written, a study on the same materials was published which supports many of the results described herein.[46]

## 3.5 References


1 J. He and T. M. Tritt, *Science*, 2017, **357**, 1369–1375.

2 Z. Ren, *Mater. Today Phys.*, 2017, **1**, 2–6.

3 L. E. Bell, *Science*, 2008, **321**, 1457–1461.

4 J. Yang and T. Caillat, *MRS Bull.*, 2006, **31**, 224–229.

5 H. J. Goldsmid and J. Sharp, *Energies*, 2015, **8**, 6451–6467.

6 J. P. Heremans, M. S. Dresselhaus, L. E. Bell and D. T. Morelli, *Nat. Nanotechnol.*, 2013, **8**, 471–473.

7 Y. Pei, Z. M. Gibbs, A. Gloskovskii, B. Balke, W. G. Zeier and G. J. Snyder, *Adv. Energy Mater.*, 2014, **4**, 1–12.

8 Y. Pei, H. Wang and G. J. Snyder, *Adv. Mater.*, 2012, **24**, 6125–6135.

9 Y. Pei, X. Shi, A. Lalonde, H. Wang, L. Chen and G. J. Snyder, *Nature*, 2011, **473**, 66–69.

10 J. Tang, B. Gao, S. Lin, J. Li, Z. Chen, F. Xiong, W. Li, Y. Chen and Y. Pei, *Adv. Funct. Mater.*, 2018, **28**, 1803586.

11 L. J. Zhang, P. Qin, C. Han, J. L. Wang, Z. H. Ge, Q. Sun, Z. X. Cheng, Z. Li and S. X. Dou, *J. Mater. Chem. A*, 2018, **6**, 2507–2516.

12 J. P. Heremans, B. Wiendlocha and A. M. Chamoire, *Energy Environ. Sci.*, 2012, **5**, 5510–5530.

13 L. Wu, X. Li, S. Wang, T. Zhang, J. Yang, W. Zhang, L. Chen and J. Yang, *NPG Asia Mater.*, 2017, **9**, e343.

14 J. R. Sootsman, D. Y. Chung and M. G. Kanatzidis, *Angew. Chemie - Int. Ed.*, 2009, **48**, 8616–8639.

15 C. Han, Z. Li and S. Dou, *Chinese Sci. Bull.*, 2014, **59**, 2073–2091.

16 L. D. Zhao, S. Hao, S. H. Lo, C. I. Wu, X. Zhou, Y. Lee, H. Li, K. Biswas, T. P. Hogan, C. Uher, C. Wolverton, V. P. Dravid and M. G. Kanatzidis, *J. Am. Chem. Soc.*, 2013, **135**, 7364–7370.

17 K. Biswas, J. He, I. D. Blum, C. I. Wu, T. P. Hogan, D. N. Seidman, V. P. Dravid and M. G. Kanatzidis, *Nature*, 2012, **489**, 414–418.

18 X. Zhou, Y. Yan, X. Lu, H. Zhu, X. Han, G. Chen and Z. Ren, *Mater. Today*, 2018, **21**, 974–988.

19 G. Ding, G. Gao and K. Yao, *Sci. Rep.*, 2015, **5**, 9567.

20 A. A. Khan, I. Khan, I. Ahmad and Z. Ali, *Mater. Sci. Semicond. Process.*, 2016, **48**, 85–94.

21 A. D. Lalonde, Y. Pei, H. Wang and G. Jeffrey Snyder, *Mater. Today*, 2011, **14**, 526–532.

22 Q. Zhao, B. Qin, D. Wang, Y. Qiu and L.-D. Zhao, *ACS Appl. Energy Mater.*, 2020, **3**, 2049–2054.

23 S. H. Yang, T. J. Zhu, T. Sun, J. He, S. N. Zhang and X. B. Zhao, *Nanotechnology*, 2008, **19**, 11–16.

24 H. S. Dow, M. W. Oh, S. D. Park, B. S. Kim, B. K. Min, H. W. Lee and D. M. Wee, *J. Appl. Phys.*, 2009, **105**, 113703.

25 S. Roychowdhury, M. Samanta, S. Perumal and K. Biswas, *Chem. Mater.*, 2018, **30**, 5799–5813.

26 M. Samanta and K. Biswas, *J. Am. Chem. Soc.*, 2017, **139**, 9382–9391.

27 K. F. Hsu, S. Loo, F. Guo, W. Chen, J. S. Dyck, C. Uher, T. Hogan, E. K. Polychroniadis and M. G. Kanatzidis, *Science*, 2004, **303**, 818–821.

28 L. D. Zhao, S. H. Lo, Y. Zhang, H. Sun, G. Tan, C. Uher, C. Wolverton, V. P. Dravid and M. G. Kanatzidis, *Nature*, 2014, **508**, 373–377.

29 S. Hao, F. Shi, V. P. Dravid, M. G. Kanatzidis and C. Wolverton, *Chem. Mater.*, 2016, **28**, 3218–3226.

30 L. Shaabani, S. Aminorroaya-Yamini, J. Byrnes, A. Akbar Nezhad and G. R. Blake, *ACS Omega*, 2017, **2**, 9192–9198.

31 Z. Huang, S. A. Miller, B. Ge, M. Yan, S. Anand, T. Wu, P. Nan, Y. Zhu, W. Zhuang, G. J. Snyder, P. Jiang and X. Bao, *Angew. Chemie Int. Ed.*, 2017, **56**, 14113–14118.

32 M. Yan, X. Tan, Z. Huang, G. Liu, P. Jiang and X. Bao, *J. Mater. Chem. A*, 2018, **6**, 8215–8220.

33 S. Roychowdhury, T. Ghosh, R. Arora, U. V. Waghmare and K. Biswas, *Angew. Chemie - Int. Ed.*, 2018, **57**, 15167–15171.

34 R. Liu, H. Chen, K. Zhao, Y. Qin, B. Jiang, T. Zhang, G. Sha, X. Shi, C. Uher, W. Zhang and L. Chen, *Adv. Mater.*, 2017, **29**, 1702712.

35 C. M. Rost, E. Sachet, T. Borman, A. Moballegh, E. C. Dickey, D. Hou, J. L. Jones, S. Curtarolo and J. P. Maria, *Nat. Commun.*, 2015, **6**, 8485.

36 C.-J. Tong, Y.-L. Chen, J.-W. Yeh, S.-J. Lin, S.-K. Chen, T.-T. Shun, C.-H. Tsau and S.-Y. Chang, *Metall. Mater. Trans. A*, 2005, **36**, 881–893.

37 B. H. Toby, *J. Appl. Crystallogr.*, 2001, **34**, 210–213.

38 A. Olin, B. Nolang, E. G. Osadchii, L. O. Ohman and E. Rosen, *Chemical Thermodynamics of Selenium, Elsevier,* 2005.

39 A. Okazaki, *J. Phys. Soc. Japan*, 1958, **13**, 1151–1155.

40 M. Sist, C. Gatti, P. Nørby, S. Cenedese, H. Kasai, K. Kato and B. B. Iversen, *Chem. Eur. J.*, 2017, **23**, 6888–6895.

41 A. Kumar, P. A. Vermeulen, B. J. Kooi, J. Rao, L. Van Eijck, S. Schwarzmüller, O. Oeckler and G. R. Blake, *Inorg. Chem.*, 2017, **56**, 15091–15100.

42 T. Ikeda, L. A. Collins, V. A. Ravi, F. S. Gascoin, S. M. Haile and G. J. Snyder, *Chem. Mater.*, 2007, **19**, 763–767.

43 H. S. Kim, Z. M. Gibbs, Y. Tang, H. Wang and G. J. Snyder, *APL Mater.*, 2015, **3**, 0145061.

44 X. Zhang, J. Shen, S. Lin, J. Li, Z. Chen, W. Li and Y. Pei, *J. Mater.*, 2016, **2**, 331–337.

45 M. Cagnoni, D. Führen and M. Wuttig, *Adv. Mater.*, 2018, **30**, 1801787.

46 D. Sarkar, S. Roychowdhury, R. Arora, T. Ghosh, A. Vasdev, B. Joseph, G. Sheet, U. V. Waghmare and K. Biswas, *Angew. Chemie Int. Ed.*, 2021, **60**, 10350–10358.

## Appendix

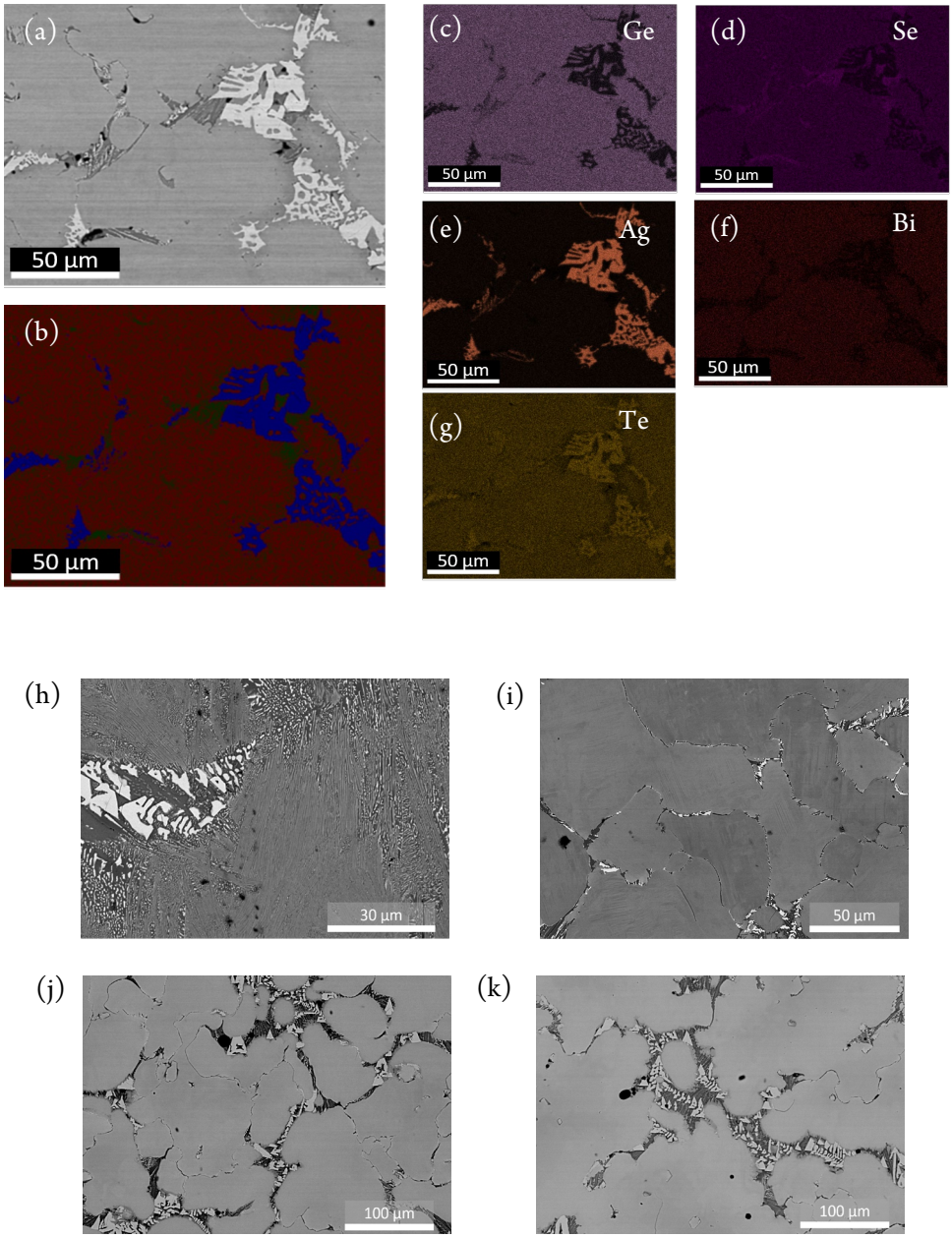


***Figure 3.10*** *(a) Back-scattered electron image, (b) phase mapping, and (c), (d), (e), (f), (g) elemental mapping of* $(GeSe)_{0.9}(AgBiTe_2)_{0.1}$ *sample. (h), (i), (j), (k) Back-scattered electron images of* $(GeSe)_{1-x}(AgBiTe_2)_x$ *with x=0.05, 0.15, 0.20, and 0.30 respectively.*